AIAA Journal
Vol. 47, No. 2, February 2009

Experimental Study of a Mach 3 Compression Ramp Interaction at $Re_\theta = 2400$

Matthew J. Ringuette,* Patrick Bookey, Christopher Wyckham, and Alexander J. Smits†
Princeton University, Princeton, New Jersey 08544

DOI: 10.2514/1.38248

Experiments were performed to investigate the flow in a Mach 2.9 shock wave turbulent boundary-layer interaction at a Reynolds number based on momentum thickness of 2400. The flow configuration was a nominally two-dimensional 24 deg compression ramp, which exhibited a separation bubble in the corner region. Mean flow quantities, including the velocity profile upstream and downstream of the corner, and the wall pressure through the interaction were measured. Filtered Rayleigh scattering was used to visualize the flow structure in the interaction and provide quantitative measurements of the turbulent structure angle and the intermittency of the boundary-layer edge turbulence. The shock motion was characterized by measuring the fluctuating wall pressure. The results indicate that, compared to previous measurements obtained at higher Reynolds numbers of 60–80,000, the separation bubble is approximately twice as long, the root mean square of the wall-pressure fluctuations has a relatively smaller peak, and the intermittency of the wall-pressure signal in the shock-foot region is attenuated. As in the high-Reynolds-number case, the shock motion has a broadband frequency distribution with a peak slightly below 1 kHz. The mean flow quantities, root mean square wall-pressure-fluctuation profile, wall-pressure signal, and shock-motion frequency agree well with the direct numerical simulation of a previous study at matching conditions.

Nomenclature

C_f = skin friction coefficient
d = transducer diameter
H = shape factor of the upstream boundary layer
n = exponent in power-law relation
p = pressure
Re_θ = Reynolds number based on freestream values and θ
r = recovery factor
T = temperature
t = time
u = velocity in the streamwise direction
u_τ = friction velocity
x = streamwise distance
y = wall-normal distance from the flat plate model
γ = intermittency function
ΔX = upstream influence parameter
δ = 99% thickness of the upstream boundary layer
δ^* = displacement thickness of the upstream boundary layer
θ = momentum thickness of the upstream boundary layer/structure angle
ν = kinematic viscosity
ρ = density
τ = shear stress

Subscripts

a = adiabatic
c = convection
w = value at the wall
∞ = freestream value

Superscripts

$+$ = normalized using inner-variable scaling
$'$ = fluctuation from the mean

I. Introduction

The shock wave turbulent boundary-layer interaction (SWTBLI) generated by a two-dimensional compression ramp displays a large separated zone when the ramp angle and Mach number are sufficiently high. Previous studies by, for example, Settles et al. [1,2], Dolling and Murphy [3], Ardonceau [4], Kuntz et al. [5], Smits and Muck [6], and Selig et al. [7], include a wide range of turning angles and cover a Reynolds number range based on momentum thickness Re_θ of about 10^4–10^5. Here, we present mean flow surveys, flow visualization, and fluctuating wall-pressure measurements for a 24 deg compression ramp at a freestream Mach number of 2.9 and a substantially smaller Reynolds number ($Re_\theta = 2400$), so that the results may be compared directly with data from direct numerical simulation (DNS) by, for example, Adams [8] and Wu and Martín [9]. To the best of the authors' knowledge, no other experimental SWTBLI data exist for a compression-ramp configuration at similar DNS-compatible Reynolds numbers.

Figure 1a shows mean wall-pressure distributions for ramp angles from 8 to 24 deg at Mach 2.85 and $Re_\theta = 67,200$ from Settles et al. [2]. Also indicated on the plot are the theoretical inviscid pressure-rise levels for each ramp angle. Incipient separation occurs at 16 deg, and, at higher ramp angles, the mean wall-pressure distribution displays a "plateau" region indicating the presence of separation [2]. The streamwise locations of the mean flow separation and reattachment lines are denoted by S and R, respectively, both determined using a surface flow visualization technique similar to that described here in Sec. III.B. For the 24 deg ramp, the time-averaged region of separation has a streamwise extent of approximately 2.1δ, where δ is the upstream, or undisturbed, boundary-layer thickness. Separation starts at about 1.6δ upstream of the corner, and reattachment occurs at approximately 0.5δ downstream of the corner. Downstream of reattachment, the wall pressure ultimately recovers to the inviscid oblique-shock value, but this occurs farther downstream with increasing ramp angle, and was not observed by Settles et al. [2] for the 24 deg ramp case due to the limited length (5δ) of their ramp model. The streamwise distance from the corner at which the mean wall pressure begins to rise due to the presence of the shock is called the upstream influence parameter,

---

Presented as Paper 4899 at the 35th AIAA Fluid Dynamics Conference and Exhibit, Toronto, Ontario, 6–9 June 2005; received 24 April 2008; accepted for publication 11 July 2008.

*Postdoctoral Research Associate, Mechanical and Aerospace Engineering Department. AIAA Member.

†Professor, Mechanical and Aerospace Engineering Department. AIAA Fellow.

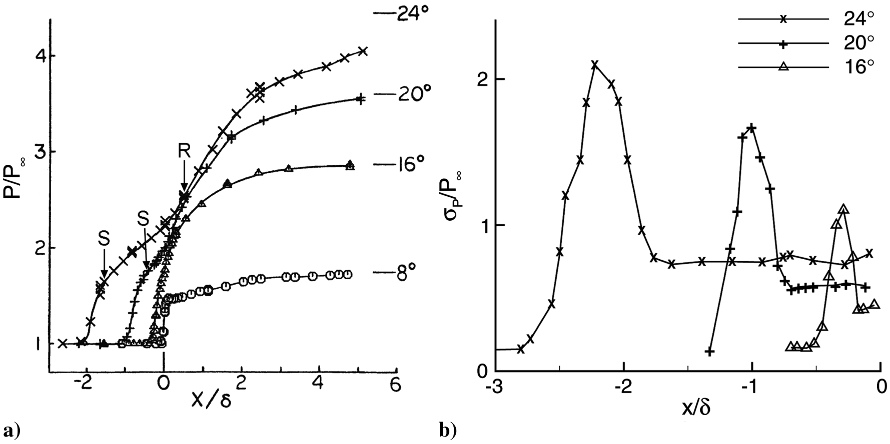

a) b)

Fig. 1 Wall-pressure measurements in compression corner interactions at Mach 3: a) mean surface-pressure distribution at different ramp angles, adapted from Settles et al. [2], $Re_\theta = 67,200$; b) standard deviation of the wall pressure, equal to $p'_{w,\mathrm{rms}}$, adapted from Muck et al. [11], $Re_\theta = 84,500$. The corner is at $x/\delta = 0$.

$\Delta X/\delta$ [1]. Settles et al. [1] investigated the effect of Reynolds number on separation in compression-ramp interactions at Mach 2.9 using two configurations: a two-dimensional compression ramp and an ogive cylinder flare model. They found that, although the angle for incipient separation did not significantly change with Reynolds number, $\Delta X/\delta$ increased with decreasing Reynolds number. At this Reynolds number, the separation shock penetrates nearly to the wall [3]. In the reattachment region, a compression fan occurs and merges with the separation shock, acting to reinforce it [2]. Smits and Muck [6] showed that the interaction amplifies both the turbulent stresses and length scales significantly, and Selig et al. [7] found that the mass-flux fluctuations increase by about a factor of 5 across the interaction.

The unsteady nature of the flow in the interaction region has been well documented. The shock generated by the compression ramp is known to oscillate randomly with a broadband frequency distribution. The frequency has a mean of about 1.5–2 kHz [3], but the maximum can be as high as 10 kHz [3,10]. These values are typically an order of magnitude less than the characteristic frequency of the large eddies in the incoming boundary layer U_∞/δ, where U_∞ is the freestream velocity. There are two primary components of the shock motion: a streamwise back-and-forth translation having an amplitude on the order of δ [3], and a large-scale, spanwise "rippling" superimposed on the translation [11]. Erengil and Dolling [12] showed that the spanwise ripples are caused by large-scale turbulent structures in the incoming boundary layer, and that they have a higher frequency and smaller streamwise amplitude than the large-scale translation (see also Muck et al. [11]). The physical mechanisms responsible for the large-scale translation are still the topic of current research. It has been suggested that features of the incoming boundary layer, such as the passage of δ-scale turbulent bulges [10] or the fullness of the mean velocity profile (fuller when the shock is downstream) [13], play a role, but more recent attention has focused on the so-called streamwise superstructures [14] or very large-scale motions [15] in the incoming boundary layer (see Ganapathisubramani et al. [16]). These motions are thought to be composed of roughly aligned groups of δ-scale coherent structures called hairpin vortex packets [15,17], and experiments and DNS at supersonic conditions used Taylor's hypothesis of "frozen" convection to infer that these structures attain lengths greater than 40δ [16–18]. The superstructures are therefore much longer than the δ-scale turbulent bulges. Similar results have been obtained for incompressible flows [14,19,20]. An alternative position holds that the streamwise shock translation is driven by the unsteady expanding and contracting of the corner separation bubble [21–24].

The rise in the mean wall-pressure distribution upstream of the plateau (Fig. 1a) is the result of the shock oscillating over the measurement region, so that the average wall pressure is a combination of the value in the undisturbed boundary layer and that behind the shock; the contribution from the shock is weighted by the amount of time it spends upstream of a given location [22]. Fluctuations in the wall pressure through the interaction are therefore due to both the incoming boundary-layer turbulence and the shock motion. Muck et al. [11] measured the unsteady wall pressure for Mach 2.9 compression ramps at various angles, and the resulting profiles of the standard deviation (equivalent to the rms of the wall-pressure fluctuations from the mean, i.e., $p'_{w,\mathrm{rms}}$) are given in Fig. 1b. The peak in the distribution corresponds to the region just upstream of the mean separation point [7]. Selig et al. [7] measured the energy spectra of the wall-pressure signal, and showed that the largest contribution to p'_w comes from the broadband, low-frequency shock oscillations.

The DNS of Wu and Martín [9], at conditions matching those of the present experiments, indicate a separation bubble length of about twice that measured by Settles et al. [2], as well as a significantly lower peak value of $p'_{w,\mathrm{rms}}$ than those obtained at high Reynolds numbers. Ringuette et al. [25] used the same DNS data to study low-Reynolds-number effects, and showed that the analysis of the fluctuating wall pressure must be done differently depending on the Reynolds number. The p'_w signal of the DNS in the shock oscillation region does not exhibit the clear intermittent behavior (between the undisturbed boundary-layer value and that behind the shock) of the high-Reynolds-number data. However, Ringuette et al. [25] found that the low-frequency shock motion and the turbulence amplification appear to be unaffected by the Reynolds number.

The Reynolds number dependence of the separation bubble length and the differences between the results given by DNS and the higher-Reynolds-number studies demonstrate the need for additional measurements at low Reynolds numbers. Here we investigate an $Re_\theta = 2400$ compression-ramp flow and compare the results with high-Reynolds-number measurements and also the DNS data of Wu and Martín [9] at matching conditions.

II. Experimental Setup

A. Facility

The experiments were conducted in the Princeton Gas Dynamics Laboratory low-turbulence variable geometry supersonic tunnel. A two-stage ejector system provides a zero-flow back pressure of about 2.41 kPa (0.35 psia) and permits the use of subatmospheric stagnation pressures. The stagnation temperature and pressure for all tests were 73 kPa (10.6 psia) and 293 K, respectively, with a run-to-run variation of less than 5%, giving a nominal freestream Reynolds number of $5.75 \times 10^6\ \mathrm{m}^{-1}$. The test section has a 200×200 mm cross section and is 920 mm in length. A flush-mounted window allows optical access from the test section ceiling, whereas a circular window 200 mm in diameter provides optical access from the side (see Bookey [26] for more details).

The boundary layer developed along a brass flat plate model, 585 mm long and 18.5 mm thick, having a sharp leading edge and spanning the width of the test section. The flat plate was nearly adiabatic ($T_w/T_{a,w} = 0.95$) under the conditions used here. The plate was positioned 51 mm below the centerline of the nozzle exit with the leading edge at the exit plane of the nozzle. The surface finish of the plate was approximately 3.18×10^{-3} mm, which is substantially smaller than the characteristic viscous length scale of the flow. A cylindrical trip wire 1.65 mm in diameter was mounted 63 mm from the leading edge to fix the transition point. Static pressure ports were located along the plate centerline. The compression ramp was a 24 deg brass wedge fitted with static pressure taps along its centerline and attached to the plate at a distance from the leading edge that could be varied from 300 to 334 mm. The ramp was 152 mm wide, and aerodynamic fences were attached at its sides to minimize flowfield three-dimensionality and avoid disturbances from the sidewall boundary layers. During filtered Rayleigh scattering experiments (Sec. II.C), one fence was removed to allow optical access.

B. Wall-Pressure Measurements

Mean wall-pressure measurements were performed with the ramp attached to the plate in two separate experiments: first, using both the plate and ramp pressure taps, and, second, using only the plate pressure taps (i.e., in the region upstream of the ramp). For the first data set, the pressures were measured using a Scanivalve Model 48J4-2141 and an MKS Baratron 133.3 kPa (1000 torr) absolute pressure transducer. For the second experiment, the same model Scanivalve was used but with a more sensitive 13.3 kPa (100 torr) MKS Baratron absolute pressure transducer. Calibration of this transducer yielded an uncertainty of slightly greater than 2% of the local mean value upstream of the interaction, which decreased to below 1% at the corner. Each data point for both experiments represents the average of 1000 samples. The results indicate excellent agreement between the two sets of measurements.

Fluctuating wall-pressure measurements were conducted within the interaction region upstream of the ramp. A single pressure transducer was used for the measurements, and data were obtained at multiple streamwise locations by positioning the compression ramp relative to the fixed transducer. Using a power-law relation [22] with $n = 7$ to empirically estimate the streamwise change in the boundary-layer thickness gives a $\pm 4.5\%$ variation in Re_δ over the 5δ range of travel of the ramp, which was considered to be acceptable. The good agreement between the mean wall-pressure distribution measured using a fixed ramp and pressure taps and that obtained from the Kulite transducer with the ramp placed at different locations supports this assertion (see Sec. III.C).

The fluctuating pressures were measured using a Kulite Semiconductor, Inc., Model XCQ-062-15A absolute pressure transducer with a piezoresistive, silicon diaphragm 0.71 mm in diameter, to which a fully active Wheatstone bridge was bonded atomically. Although the natural frequency of the pressure-sensing diaphragm was about 200 kHz, the diaphragm was recessed 1.9 mm below a protective screen so that a standing wave in the 50–80 kHz range was excited in the cavity. This limited the frequency response of the transducer to about 50 kHz, which was deemed sufficient for capturing the frequencies associated with the shock motion. The transducer was calibrated statically, and the shock tube tests of Raman [27] demonstrate that diaphragm-type transducers have dynamic calibrations only a few percent lower than those obtained statically. To minimize power supply noise, the transducer was powered using batteries. The output from the transducer was amplified by a Dynamics Model 7525 amplifier and was low-pass filtered at 50 kHz with an Ithaco Model 4213 fourth-order Butterworth filter. A National Instruments Model 6040E 12-bit A/D converter was used to acquire the transducer signal at a sampling frequency of 100 kHz. For each test, 1.5 million data points were taken; convergence in the mean and standard deviation was ensured by comparison with data from twice the number of samples. Calibration of the Kulite transducer gave an uncertainty of slightly less than 8% of the local mean wall pressure upstream of the interaction, which decreased to about 4% at the start of the interaction and to below 3% at the corner.

It was critical that the transducer be positioned flush with the surface of the plate [28]. The transducer was therefore mounted into a hollowed-out #6-32 machine screw for height adjustment, which had a nonthreaded portion at the measurement end to facilitate proper alignment as it was screwed into the plate from underneath. The transducer flushness was inspected by viewing the assembly under magnification, and the error was estimated to be within 2 viscous units (<40 μm). Care was taken to ensure that any departure from flushness resulted in the transducer being slightly recessed rather than raised, which, according to Dolling and Dussauge [28], creates significantly less error than a protruding sensor.

The sensing diameter of the Kulite transducer was about 11% of δ, so that the pressure measurement at a given location was subject to spatial integration. The effect of this integration on the frequency response can be estimated using the analysis of Dolling and Dussauge [28]. At Mach numbers below 5, it can be assumed that the statistical nature of the pressure signal in zero pressure gradient boundary layers is similar to that at subsonic speeds. For subsonic flows, Corcos [29] showed that the frequency at which 3 dB damping occurs for a transducer of diameter d is approximately $U_c/\pi d$, where U_c is the convection velocity of the pressure perturbation. Near the wall, the convection velocity of the turbulent boundary-layer structures is typically about $0.6U_\infty$, so that the 3 dB damping frequency for the present Kulite transducer was estimated to be about 162 kHz. This value is larger than the highest resolvable frequency of the transducer (50 kHz), so that spatial integration effects were not considered to be significant. The large-eddy frequency for the upstream boundary layer U_∞/δ was about 90 kHz. Therefore, the Kulite transducer was not able to resolve the pressure fluctuations due to the boundary-layer turbulence. However, the frequency of the shock motion in the interaction region will be shown to be on the order of 1 kHz, similar to the value at high Reynolds numbers, and, therefore, the Kulite transducer was considered adequate for characterizing the large-amplitude, low-frequency pressure fluctuations due to the shock motion.

C. Filtered Rayleigh Scattering

To visualize the flow structure in the interaction, CO_2-enhanced filtered Rayleigh scattering (FRS) was used. Rayleigh scattering is the scattering of light from particles that have a characteristic size on the order of (or less than) the wavelength of the incident light. Here, CO_2 gas was injected upstream of the stagnation chamber with a mass flux of about 1.0% of the tunnel air mass flux. As the air–CO_2 mixture expands through the tunnel nozzle, the CO_2 condenses and forms clusters that Erbland [30] estimated to be on the order of 10 nm. These clusters significantly enhance the molecular Rayleigh signal. When the CO_2 clusters are entrained into the boundary layer, aerodynamic heating effects (confined to the boundary layer) cause their temperature to increase above the sublimation value so that the condensate vaporizes. The boundary layer therefore appears as a region of low-intensity scattering, surrounded by high-level scattering (bright regions) corresponding to the freestream fluid. Previous experiments showed that the interface between the heated boundary-layer fluid and the cold freestream flow is well-represented by the intensity differences in the Rayleigh scattering signal, primarily because the time scale of the CO_2 sublimation is small compared to the characteristic time scale of the entrainment process [31]. Because the signal from the moving particles is Doppler shifted by an amount that depends on the angle of viewing, a narrowband molecular filter may be used to attenuate the background scattering from the (stationary) tunnel walls.

The optical arrangement for the FRS imaging is shown in Fig. 2. The flow was imaged in a streamwise, wall-normal plane in the interaction region. For illumination, a Spectra Physics Q-switched, injection-seeded, frequency-doubled, pulsed Nd:YAG laser was used. The pulse frequency was 10 Hz and the pulse duration was 10 ns, and, for single-image FRS, the energy of each pulse was about 100 mJ at a wavelength of 532 nm. The laser was tuned to a frequency in the absorption band of the molecular filter. The filter was a glass cell filled with iodine vapor, and the vapor pressure was controlled by

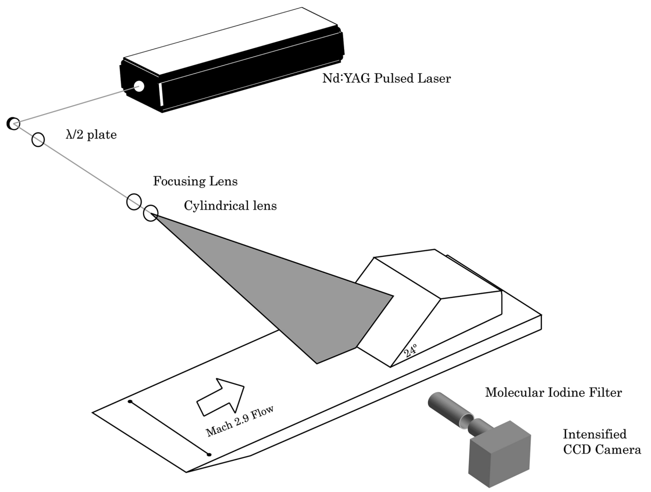

Fig. 2 Optical setup for flow imaging using filtered Rayleigh scattering.

a hot water bath at 50°C (for details, see Bookey [26]). Several first-surface mirrors were employed to direct the beam into the test section, and a single half-wave polarizer was used to orient the polarization of the light so that the scattering in the plane of the camera was maximized. A focusing lens and a cylindrical lens were used to adjust the beam width and spread it into a sheet, respectively, and the sheet thickness was about 100 μm in the imaging region; the centerline of the sheet was oriented at 135 deg to the mean flow vector.

The flow was imaged using a double-intensified charge-coupled device (CCD) camera with a 100 mm focal length f/4.5 lens, and the camera output was recorded using a commercial-grade SVHS recorder. The SVHS videotapes were digitized using Final Cut Pro software by Apple, and still images were grabbed from the video at a resolution of 720 × 480 pixels. MATLAB was used to postprocess the still images. The images were cropped to include only the areas of interest, low-pass filtered to remove noise, and the contrast between the darker region denoting the boundary layer and the bright areas indicating the freestream flow was enhanced using a histogram stretch.

III. Results

A. Upstream Boundary Layer

To obtain the mean velocity, density, and Mach number profiles in the undisturbed boundary layer, mean pressure and temperature surveys were conducted using a pitot probe and a total temperature probe, respectively, at a location 340 mm downstream of the plate leading edge. The pitot probe had a flattened tip 2 mm wide with a 0.3-mm-high opening and an outer, vertical dimension of 0.76 mm. Because of the short run times available and the low pressures being measured, a relatively large probe opening was required to provide acceptable time response at the cost of spatial resolution.

Figure 3a shows the resulting streamwise mean velocity profile, normalized by the freestream velocity and plotted versus distance from the wall scaled by δ; y denotes wall-normal distance as measured from the flat plate model and u is the streamwise velocity. Also plotted is the mean velocity profile from the DNS of Wu and Martín [9]. There is good agreement between the experiments and the simulation, except near the wall for $y/\delta < 0.2$, due to probe errors discussed next.

The mean streamwise velocity u^+, transformed using the method of van Driest [32], but with a nonunity recovery factor (i.e., van Driest II) determined from the experiments to be $r = 0.87$, is plotted versus y^+ on a linear-log plot in Fig. 3b. The superscript ($^+$) indicates normalization using inner, or wall, variables: u_τ for velocity and ν_w/u_τ for length, where $u_\tau = \sqrt{\tau_w/\rho_w}$ is the friction velocity, ν_w is the kinematic viscosity at the wall, τ_w is the wall shear stress, and ρ_w is the density at the wall. The mean wall shear stress was obtained using the Clauser chart method [33]. The skin friction coefficient, $C_f \equiv 2\tau_w/\rho_\infty U_\infty^2$, was found to be 0.00217. The error in the Clauser chart method can be significant. Clauser chart values for wall shear stress are typically 5% higher than Preston tube measurements, which are themselves 6–11% higher than the estimates using the method of Spalding and Chi [34].

The transformed velocity shows a well-defined turbulent profile with small logarithmic and wake regions characteristic of a low-Reynolds-number turbulent boundary layer. For $y^+ < 70$, the data fall below the logarithmic-law reference line. This behavior is not thought to be the start of the buffer region, but is most likely due to errors in the pitot probe measurements, to be discussed next. Also plotted in Fig. 3b is the van Driest transformed velocity profile from the DNS of Wu and Martín [9]. There is good agreement between the experimental profile and that of the simulations for $70 < y^+ < 150$, although the velocity for the experiments overshoots that of the DNS near the boundary-layer edge. For the DNS, C_f was found to be 0.00217, which matches that of the experiments. Although this agreement is excellent, it is probably fortuitous because the use of the Clauser chart method, coupled with the small number of points available to fit to the logarithmic law, introduces significant uncertainty in the experimental value.

The discrepancies between the present data and both the logarithmic law and the DNS are most likely due to pitot probe measurement errors. Allen [35] describes the disturbance effects of large probes near the wall in supersonic flow. The bow shock in front of the probe may cause local separation of the boundary layer upstream of the probe. Also, near the wall, the bow shock may not be normal to the probe, which was assumed in the analysis of the probe measurements. Allen reports that wall effects are essentially confined to about one probe diameter away from the wall. For the present experiments, the measurements for $y^+ \geq 70$ are believed to be free from substantial wall effects. This distance is about 1.4 mm away from the wall, which is nearly twice the outer probe dimension.

Allen [35] also discusses "probe displacement" errors, where the effective probe measurement location is displaced from the geometric center. By convention, positive displacement indicates

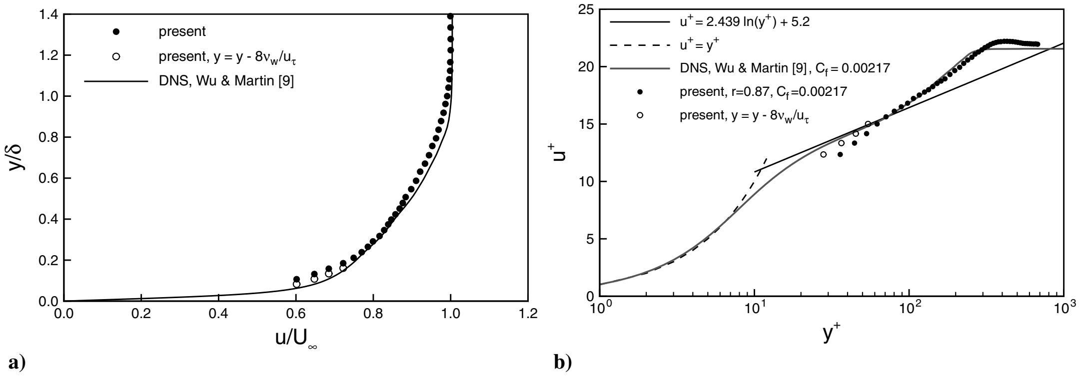

Fig. 3 Mean velocity profiles in the upstream boundary layer, compared with the DNS data of Wu and Martín [9] at matching conditions: a) outer scaling; b) van Driest transformed velocity; the Clauser chart method [33] is used to obtain C_f for the experiments.

that the reported probe position must be increased to obtain the true velocity profile. Away from the wall, Allen found displacement effects to be small and relatively constant, with positive displacements of approximately 40% of the probe diameter, for circular probes having diameters less than 15% of δ; the vertical dimension of the present pitot probe (a flattened probe) was about 11% of δ. However, Allen reported that, near the wall (within approximately one probe diameter), the displacement decreases and may even become negative.

For the present data to follow the logarithmic law and the DNS data more closely, a negative shift (to account for negative displacement) must be applied to the y locations of the data for $y^+ \leq 62$. To examine the displacement effects, a distance of half of the vertical probe opening, approximately eight viscous length scales, was subtracted from the y positions of the four data points closest to the wall. These shifted data points are shown as open circles on the outer-scaled velocity plot and the transformed velocity profile, Figs. 3a and 3b, respectively. This negative shift in the y location causes the original point at $y^+ = 62$ to fall onto the reference line for the logarithmic law. However, it is clear that the displacement effect of the probe is not constant with distance from the wall, as this value does not collapse the data closer to the wall. This is not surprising, because the near-wall distortion of the pitot probe bow shock and the local boundary layer, described earlier, imply that the shock distortion and probe displacement effects cannot be decoupled.

Table 1 gives the parameters for the incoming boundary layer for the present experiments, using the data with no corrections for pitot probe errors, as well as the DNS of Wu and Martín [9]. Included are the boundary-layer thickness where u is 99% of the freestream value δ, the displacement thickness δ^*, θ, the shape factor $H = \delta^*/\theta$, Re_θ, and C_f. In general, there is good agreement between the experiments and the simulations, although δ^* is somewhat higher for the experiments. This may be due to the probe errors as discussed earlier.

B. Flow Visualization

The mean streamline patterns near the surface of the 24 deg compression corner interaction were visualized using the oil-flow technique (see Settles [36], Appendix B, for a detailed description of a similar technique). The oil used was Dow Corning 200® silicone, which was colored using graphite particles ranging in size from minute particles to small granules on the order of 0.025 mm (0.001 in.) in diameter. To keep the viscosity of the mixture low, the silicone oil and graphite particles were combined in a ratio of about six parts to one. Upstream of the ramp, this mixture was applied to the plate in a spanwise-oriented row of equally spaced dots over a distance encompassing most of the ramp width. On the ramp surface, the mixture was applied in a grid of discrete dots to highlight details in the interaction. The dots did not move down the ramp before the tunnel start, as long as the tunnel was run shortly after application. When the tunnel was started, the wall shear stress caused the dots upstream and downstream of the interaction to stream down the model surface, coating it and forming a streaky pattern. Within about 20 s of the tunnel starting, the mixture flowed through the interaction region and revealed surface streamline patterns. Flow separation is indicated by an accumulation of graphite particles at a line of convergence. A Canon Elura progressive scan CCD camcorder was used to record the run to digital video, thus capturing the development of the surface flow in real time. Video was used to ensure the acquisition of flow images before any distortions that the tunnel shutdown might cause.

The resulting oil-flow pattern is given in Fig. 4. It was assumed that the lines of convergence and divergence closely matched the mean separation and reattachment lines. The average location of separation is about 3.2δ upstream of the corner, and reattachment occurs about 1.6δ downstream of the corner. The total length of the separated zone is therefore approximately 4.8δ, a little higher than the maximum value given by the correlation of Zheltovodov et al. [37] at this Mach number. This value is also more than twice as large as that found by Settles et al. [2] using a 24 deg corner at the same Mach number but at $Re_\theta = 67,200$, so that the extent of the separation bubble increases significantly at lower Reynolds numbers.

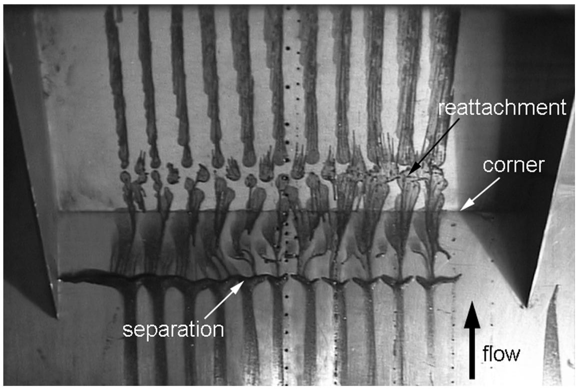

Fig. 4 Surface flow visualization of the 24 deg compression-ramp interaction, using a mixture of silicone oil and graphite.

Figure 4 also reveals the three-dimensional nature of the interaction. The combination of the curvature of the spanwise separation line and the alternating direction of curving surface lines in the separated region most likely indicates the presence of pairs of counter-rotating streamwise vortices [22]. It is difficult to make any conclusions about the change in three-dimensionality of the interaction with Reynolds number based on previous results. Selig [38] shows surface visualizations of the separated corner flow from four different investigators using the same wind tunnel at nominally the same conditions with the same model configuration (Mach 2.84, 24 deg ramp). The striking result is that the details indicating a departure from nominally two-dimensional flow are different in each visualization. After changing many features of his experimental setup with little effect on the flow pattern, Selig [38] concluded that the details of the three-dimensional structure of the separation bubble are very sensitive to the initial conditions, or upstream flow, in the tunnel.

C. Mean Wall Pressure

The mean wall-pressure distributions, as measured using the wall-pressure taps and the Kulite transducer, are shown in Fig. 5; the theoretical inviscid value for the pressure rise downstream of the shock is marked using a horizontal line in the figure. Also plotted are the results from the DNS data of Wu and Martín [9] and the high-Reynolds-number measurements of Settles et al. [2] at Mach 2.85; the ramp angle for both studies is 24 deg. The pressure distribution of the present experiments is only qualitatively similar to the higher-Reynolds-number data. There is a rise in pressure in the shock oscillation region, followed by a plateau farther downstream, which is indicated by an inflection point at approximately $x/\delta = -2.25$ (the corner is at $x = 0$). The measurements of Settles et al. [2] show a separation region that is a factor of 2 smaller than that of the low-Reynolds-number experiments and the DNS data. This is consistent with the flow visualization results presented in Sec. III.B. Figure 5 indicates generally good agreement between the low-Reynolds-number experiments and the DNS data at the same conditions.

The present data also show that the pressure rise across the shock overshoots the inviscid value by about 6% at $x/\delta = 8.4$, finally

Table 1 Properties of the upstream boundary layer

	M	Re_θ	δ, mm	δ^*, mm	θ, mm	$H = \delta^*/\theta$	$C_f \times 10^3$	u_τ, m/s
Experiment	2.9	2400	6.7	2.36	0.43	5.49	2.17	32.9
DNS [9]	2.9	2300	6.4	1.80	0.38	4.74	2.17	34.0

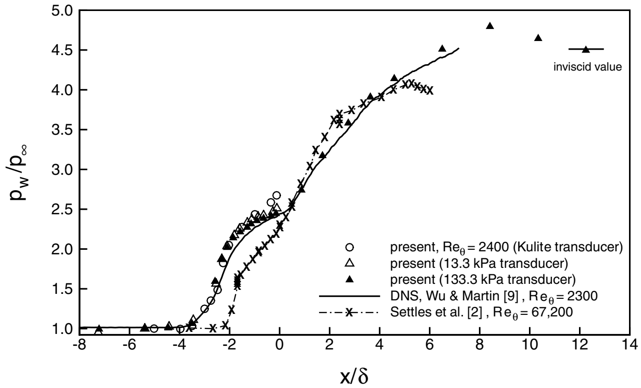

Fig. 5 Mean wall-pressure at low and high *Re* for a 24 deg ramp at Mach 3, normalized by the undisturbed boundary-layer pressure p_∞. The corner is at $x/\delta = 0$, a horizontal line marks the inviscid pressure-rise value.

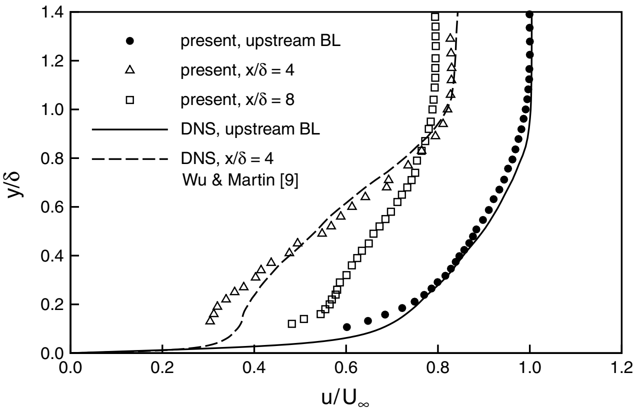

Fig. 6 Mean velocity profiles in the interaction region compared with the DNS data of Wu and Martín [9] at matching conditions.

recovering to the inviscid value at $x/\delta = 12.25$. At present, there is no definitive explanation for this overshoot. It does not seem likely that the boundary layers on the fences are significantly affecting the flow two-dimensionality and causing the overshoot, as the ramp width is relatively large (about 23δ) and the surface flow visualization (Fig. 4) indicates that the flow is highly two-dimensional upstream and downstream of the unsteady interaction. The pressure peak may be real. Given that the separation and reattachment shocks intersect well above the boundary layer, there will be a set of compression waves that originate near this intersection and propagate toward the wall, where it will reflect and raise the pressure before the final relaxation takes place. Although these waves are weak, they may well lead to an overshoot in the wall pressure above the inviscid asymptote. The DNS also shows shocklets emanating from the turbulent boundary-layer structures near the reattachment line, downstream of the corner. The existence of these wave phenomena, coupled with the experimental error, does not rule out the possibility of an overshoot in the pressure ratio before the recovery to the inviscid value.

No comparison of this overshoot with the DNS pressure profile is possible, as the simulation does not extend beyond 7.2δ from the ramp corner. However, a less-pronounced overshoot was found by Dolling and Murphy [3], who measured the mean wall pressure along a 24 deg ramp at Mach 2.95 using a Kulite transducer (figure 4a in their paper). They found that, for their most downstream data points along the ramp, $x/\delta = 5.8$ and 6.8, the mean wall-pressure ratios were about 3% and 4% higher, respectively, than the inviscid value. These authors also used fences on either side of the ramp model. They did not comment on these discrepancies, only mentioning that their data are closer to the inviscid value than that of Settles [1], who reported a pressure ratio lower than the inviscid prediction, primarily because their data did not extend far enough along the ramp.

The two Kulite transducer data points closest to the corner are about 6% higher than the pressure values obtained using the wall-pressure taps. Selig et al. [7] plotted mean wall-pressure measurements of four different studies done in the same wind-tunnel facility at similar conditions, also using Kulite transducers, and found discrepancies that exceeded 10%. These differences could be due to spanwise variations in flow conditions associated with the flow three-dimensionality, because the Kulite transducer is offset in the spanwise direction from the row of wall-pressure taps by 2δ (9% of the ramp width). The flow visualization given in Fig. 4 indicates a small amount of spanwise flow in the interaction region.

D. Velocity Profiles

Mean velocity profiles were obtained at 4δ and 8δ downstream of the corner using the pitot probe described earlier. The total temperature profile was estimated by interpolating the profile from the undisturbed boundary layer. The resulting velocity profiles, nondimensionalized by U_∞ in the upstream boundary layer (BL), are given in Fig. 6. Also plotted is the velocity profile from the DNS of Wu and Martín [9] at $x = 4\delta$; the DNS data do not extend to $x = 8\delta$. Figure 6 shows that, at 4δ downstream of the corner, the flow in the boundary layer is attached but remains highly retarded near the wall. This profile is in good agreement with that of the DNS, except near the wall where the errors from the pitot probe are significant. The velocity profile at $x = 8\delta$ indicates a rapid filling out of the profile, most likely due to enhanced turbulent mixing from the formation of large-scale eddies [5], but the flow has not completely recovered at this location. Additionally, the gradual decrease in the boundary-layer edge velocity from $x = 4\delta$ to 8δ corresponds to the gradual pressure rise observed in the surface-pressure distribution, indicating that the flow at these locations is still turning and decelerating in the final stages of the compression.

E. Filtered Rayleigh Scattering

Typical, post-processed images from FRS taken in the interaction region are given in Fig. 7. The images show two distinct diagonal lines, the most upstream of which is the leading edge of the aerodynamic fence. The bright region downstream of this leading edge is due to the incident laser light on the ramp reflecting off the fence. This light was not attenuated by the filter as expected, and is most likely due to a secondary mode of the laser light. The bright diagonal line downstream of the fence is the shock wave, and the images show a significant loss of signal downstream of the wave as the temperature rises to a level greater than the sublimation temperature of the carbon dioxide. Some of the images show the separation shock penetrating nearly halfway into the boundary layer (Fig. 7d). The penetrations appear to occur through incursions of the freestream fluid and through the turbulent structures. Other images indicate that the shock "wraps" around the large-scale turbulent bulges (Fig. 7a). This distortion of the separation shock by the upstream large-scale structures is consistent with the results of Erengil and Dolling [12], who showed that the high-frequency jitter in the shock motion is due to large-scale turbulent eddies convecting into the interaction. The compression of the boundary layer due to the shock wave can be seen in Fig. 7c, which indicates a reduced boundary-layer thickness downstream of the shock.

F. Intermittency

The intermittency function γ was estimated using the FRS images. Here, γ is the fraction of the flow at a given height in the boundary layer that is turbulent; $\gamma = 1$ indicates fully turbulent flow and $\gamma = 0$ denotes nonturbulent flow. In the FRS images, the turbulent boundary-layer fluid is represented by the darker regions, whereas the nonturbulent freestream flow is represented by brighter areas. Distinguishing between the two in the 8-bit, grayscale images was done using a pixel intensity threshold. Pixels with intensity values below the threshold were assigned a value of 255, or white ($\gamma = 1$), and those above it were given a value of 0, or black ($\gamma = 0$). The intermittency was calculated in each row of pixels, that is, at each

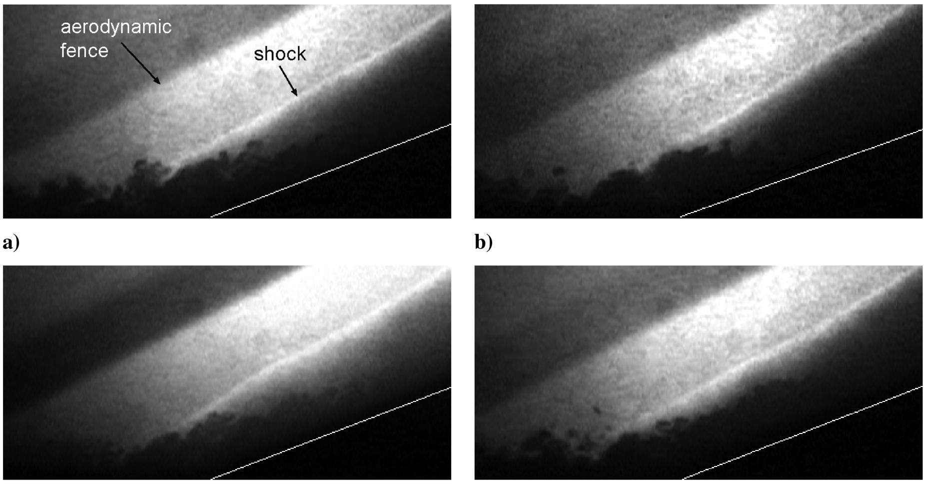

a) b) c) d)

Fig. 7 Instantaneous FRS images, uncorrelated. Images are 7.0δ x 3.3δ, with flow from left to right. The white line indicates the ramp; the flat plate is located at the bottom edge of the images.

wall-normal location, by averaging the thresholded pixel values in that row.

The pixel intensity threshold was determined by visually comparing the thresholded (black and white) images with the originals, until the threshold that best captured the interface between the boundary-layer and freestream fluid was found. Figure 8a shows an FRS image taken in the upstream boundary layer with three thresholded images below it, using pixel thresholds of 55, 65, and 75. The threshold of 65 yields the best qualitative representation of the interface between the turbulent and nonturbulent fluid, and was chosen for the present analysis. Smaller and larger threshold values may cause finer features of the interface to be lost or to blur together, respectively. Based on such visualizations, the uncertainty of the pixel threshold value was taken to be ± 10. Figure 8b plots the resulting intermittency profiles calculated using each of the three pixel intensity thresholds, averaged over 100 images. The figure shows that the uncertainty in the pixel intensity threshold of ± 10 translates to an uncertainty in γ of about $+13\%$ and -16% at the wall-normal position where γ is approximately 50% ($y_{50\%}$). For the pixel threshold value of 65, $y_{50\%}/\delta = 0.77$, which is in excellent agreement with that measured by Klebanoff [39] in an incompressible boundary layer at $Re_x = 4.2 \times 10^6$.

For the undisturbed boundary layer, γ was determined by averaging the results from 100 thresholded images with a streamwise, wall-normal field of view of $5\delta \times 1.5\delta$. As discussed in Sec. III.E, the FRS signal deteriorates significantly downstream of the shock so that γ could only be evaluated upstream of the corner. The intermittency in the interaction was computed using $1\delta \times 1.5\delta$ subimages from an ensemble of 150 images, centered on $x = -1.5\delta$ and $x = -0.5\delta$. The local boundary-layer thickness at these streamwise locations was unknown, and so γ for each case was normalized by $y_{50\%}$. In the upstream boundary layer, $y/y_{50\%} = 0.80$, increasing to 0.85 at $x = -0.5\delta$.

Figure 9a gives γ at each streamwise location. The plot shows that the magnitude of the slope of γ near $y_{50\%}$ increases relative to the upstream boundary-layer value at $x/\delta = -1.5$, then reduces slightly at $x/\delta = -0.5$. An increase in magnitude of the slope of γ indicates a smaller region of intermittent flow. However, for $y/y_{50\%} < 1.1$, these differences fall within the uncertainty in computing γ, making it difficult to draw strong conclusions from the data.

G. Structure Angle

The mean structure angle θ in the (x, y) plane was determined using spatial correlations of the FRS images at different wall-normal locations, or origin points, throughout the boundary layer. Here, θ is defined as the average local angle of the large-scale coherent structures relative to the wall, determined at a specified wall-normal location. This definition is consistent with that of Spina et al. [40], who performed correlation experiments using hot-wire probes in a

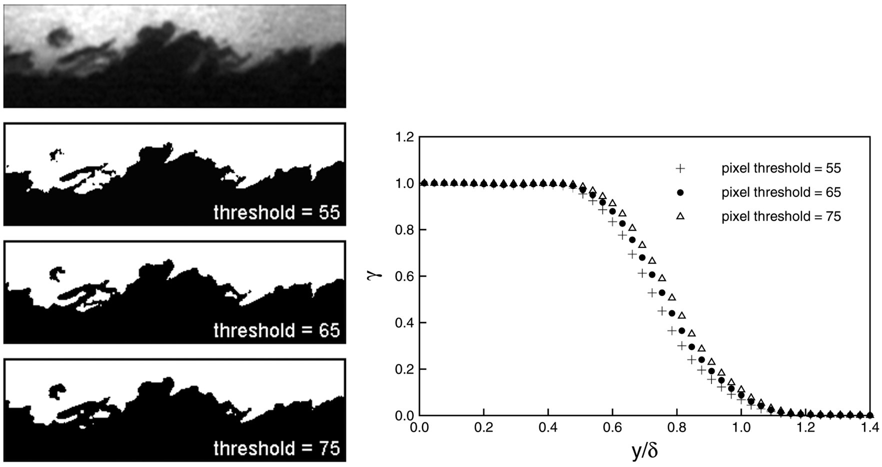

a) b)

Fig. 8 Effect of pixel intensity threshold on the intermittency function γ for the incoming boundary layer: a) original image with thresholded images in descending order; b) γ calculated from the thresholded images.

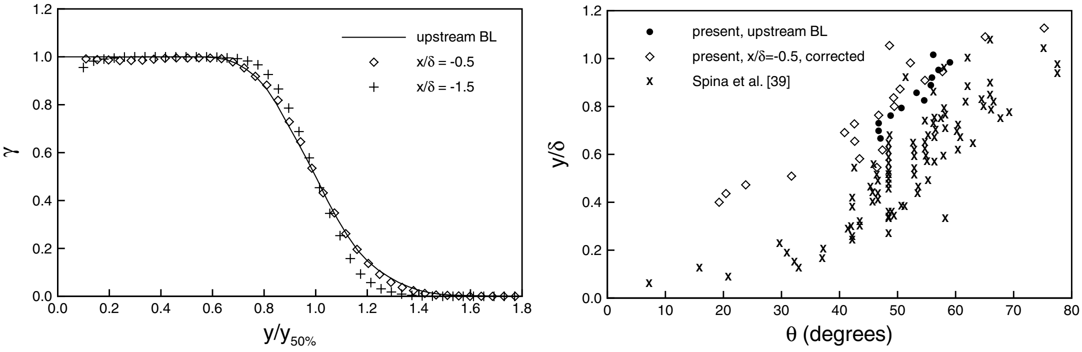

a) b)

Fig. 9 Compression-ramp interaction properties: a) intermittency function; b) mean structure angle, relative to the local surface inclination. The hot-wire data of Spina et al. [40] for a flat plate boundary layer at Mach 3, $Re_\theta = 81,000$ are shown for comparison.

high-Reynolds-number, Mach 2.9 flow. Figure 10a shows a sketch that illustrates the physical interpretation of the local θ for an individual large-scale structure in an FRS image of the undisturbed boundary layer. The FRS images show that the structures typically lean downstream (see Figs. 8a and 10a), so that the average θ is acute. Spina et al. [40] point out that the average structure angles determined using unconditional correlation methods, such as that presented here, include contributions from many types of structures at different angles. Therefore, information about individual structure properties is lost in the averaging.

The spatial correlations to obtain θ from the full FRS images were computed from the same set of FRS images used to obtain γ. For the undisturbed boundary layer, the $5\delta \times 1.5\delta$ images were divided in the streamwise direction into three $1.5\delta \times 1.5\delta$ windows, yielding 300 independent samples. This streamwise window width was deemed sufficient, as the correlations drop off to below 0.4 within the window. Because of the loss of FRS signal downstream of the shock, the structure angle in the interaction region could only be determined upstream of the corner. Within the interaction, correlations were performed using a window with a streamwise width of 1δ centered at $x = -0.5\delta$ and a height of 1.5δ.

For each window, a two-dimensional, spatial autocorrelation was performed between the pixel intensity value at a given origin point and that at every other point in the image. The correlations from each independent window were averaged to produce a mean correlation profile. The origin points were centered in the streamwise direction, but were varied in the wall-normal direction to obtain θ at different distances from the wall. An example of an average correlation for the undisturbed boundary layer, with an origin point located at $y/\delta = 0.75$ from the wall, is shown in Fig. 10b; the correlation coefficient is mapped into seven bins, specified in the caption. The figure shows that the isocorrelation contours at this height appear tilted, indicating that the structures lean toward the wall, as mentioned earlier. To determine θ, ellipses were fit to the isocorrelation contours using a direct least-squares-fitting method developed by Fitzgibbon et al. [41]. The technique was applied using contour levels of 0.7, 0.8, and 0.9 for correlations at each wall-normal location, and θ was taken as the average of the angles determined from each contour level with respect to the wall. The dashed line in Fig. 10b indicates, qualitatively, the definition of θ on the correlation map. For origin points below $y/\delta = 0.6$, the correlations degraded significantly and no angle measurements could be gathered; this cutoff decreased to about 0.4 in the interaction.

The average structure angles in the incoming boundary layer and at $x = -0.5\delta$, within the interaction, are shown in Fig. 9b. Also plotted are the $Re_\theta = 81,000$, Mach 2.9 data of Spina et al. [40] for a flat plate flow, where the angles were obtained using the space–time correlation between two hot-wire probes with various vertical separations. The angles for the present study were determined relative to the flat plate, so that the values at $x = -0.5\delta$ were corrected to take into account the turning of the flow through the shock wave. The mean angle of the separation shock was measured using correlations from the FRS image data with the reference point varied through the estimated shock location. This analysis yielded an average shock angle of 28 deg, which corresponds to a turning angle of 9.9 deg for an upstream Mach number of 2.9; this turning angle was subtracted from the measured θ at $x = -0.5\delta$.

Figure 9b shows that θ in the undisturbed boundary layer agrees reasonably well with the lower range of angles measured by Spina et al. [40]. These data suggest that the variation in θ with Reynolds number, if any, is not significant. Comparing θ in the upstream boundary layer with the corrected angles at $x = -0.5\delta$ indicates a decrease in θ of up to about 7 deg. Donovan et al. [42] investigated a high-Reynolds-number boundary layer perturbed by concave wall curvature, and observed a decrease in structure angle at the initial stages of compression, followed by an increase over the undisturbed boundary-layer value farther downstream. This is in agreement with the current results obtained upstream of the corner. Additionally, the present data show an increase in θ with distance from the wall in the outer region of the boundary layer, consistent with the measurements of Spina et al. [40].

H. Fluctuating Pressure

The rms of the fluctuating wall pressure, normalized by the local mean wall pressure p_w is plotted in Fig. 11. The DNS results of Wu and Martín [9] are also included, along with the measurements of Selig et al. [7] at $Re_\theta = 84,500$. All data given are for a 24 deg corner angle at a Mach number of about 3. Figure 11 shows that, compared with the low-Reynolds-number data, the $p'_{w,\mathrm{rms}}$ profile from Selig et al. [7] exhibits significant differences. First, the peak value for the high-Reynolds-number study is about a factor of 2 larger than that of the present experiment; this result will be discussed next. Second, the location of the $Re_\theta = 84,500$ peak is farther downstream than those of the low-Reynolds-number cases, consistent with the smaller extent of the separation bubble.

Figure 11 shows that the trends in $p'_{w,\mathrm{rms}}$ of both the present experiment and the DNS agree well, although the peak location for the DNS is about 0.2δ farther downstream. However, the most prominent difference between the current measurements and the DNS results is that the $p'_{w,\mathrm{rms}}$ curve for the DNS is consistently higher. Moreover, the difference between the two studies is amplified by a factor of about 1.6 through the shock wave. This difference may be explained by considering two different factors: added "noise" in the wall-pressure data of the DNS, and the low-pass filtering of the experimental data at 50 kHz.

The fluctuating pressures for the DNS are higher than that of the experiment due to uncorrelated pressure fluctuations (noise) introduced by the initialization of the simulation.[‡] Therefore, the fluctuating pressure at the wall is thought to be the sum of the true value p'_w and that due to noise p'_n, such that the mean square of the total signal is $\overline{(p'_w + p'_n)^2} \approx \overline{(p'_w)^2} + \overline{(p'_n)^2}$, where the product $2\overline{p'_w p'_n}$ has been neglected because the signals are uncorrelated. An

---

[‡] Martín, M. P., and Wu, M., Princeton University, Princeton, NJ. Private communication, 2007.

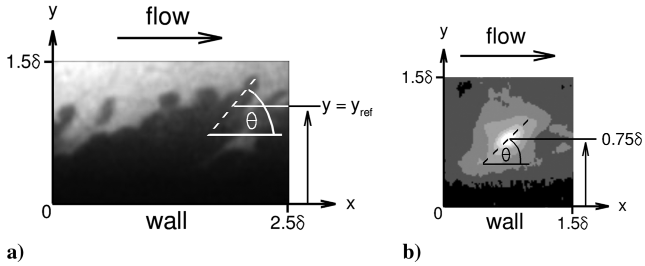

Fig. 10 Illustration of the method to determine θ from FRS images: a) sketch showing θ for an individual large-scale coherent structure at $y = y_{\mathrm{ref}}$; b) isocontours of the spatial autocorrelation used to calculate θ at a given wall-normal location. Contour levels, ranging from black to white, are 0–0.2, 0.2–0.4, 0.4–0.6, 0.6–0.7, 0.7–0.8, 0.8–0.9, >0.9. See text for description.

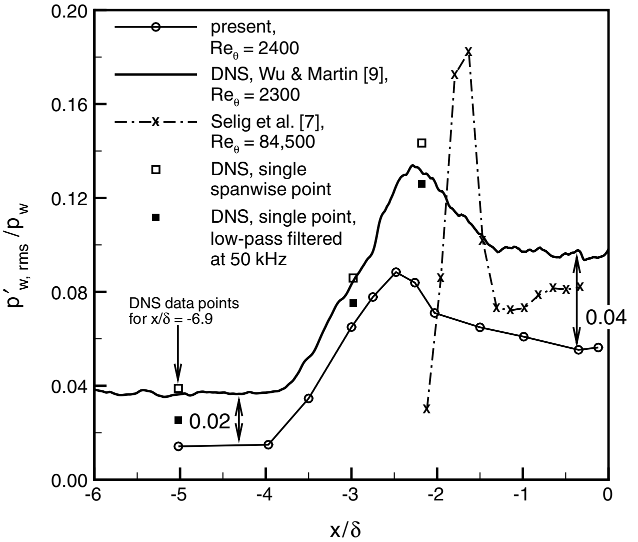

Fig. 11 Distributions of $p'_{w,\mathrm{rms}}$ at low and high Reynolds numbers for Mach 3, normalized by the local mean wall pressure p_w. See text for description. The corner is located at $x/\delta = 0$.

estimate of p'_n can be made by assuming that it is equal to the value of the fluctuating pressure in the freestream p'_∞, so that the amplification of $\overline{(p'_n)^2}$ through the shock can be estimated by finding the amplification of $\overline{(p'_\infty)^2}$ (see also Ringuette et al. [25]). The freestream value is used because it should, ideally, be largely free from pressure fluctuations aside from those introduced by the turbulent structures near the boundary-layer edge, and thus the average fluctuations in the freestream provide an approximate reference for the uncorrelated noise in the pressure field of the DNS. The freestream values for the DNS were obtained at a distance of about 2δ away from the wall. Upstream of the shock, $\overline{(p'_\infty)^2}/p_w^2$ is about 0.0004, whereas it is approximately 0.0016 downstream (although the latter value may contain some contribution due to the influence of shocklets[‡]).

Using these values to estimate the normalized mean square of the noise $\overline{(p'_n)^2}/p_w^2$ gives an amplification factor of 4 through the shock, so that the rms of the noise is amplified by a factor of 2. This is in reasonable agreement with the value of 1.6 given earlier. Using the estimate of $\sqrt{\overline{(p'_n)^2}}/p_w$ to approximate the increase due to noise in the normalized rms of the total signal $\sqrt{\overline{(p'_w + p'_n)^2}}/p_w$ yields 0.02 upstream of the shock and 0.04 downstream. Both values are indicated in Fig. 11 and are good estimates of the differences between the experimental and DNS curves.

The low-pass filtering of the present fluctuating wall-pressure measurements at 50 kHz will also account for some of the difference between the experimental and DNS curves of $p'_{w,\mathrm{rms}}$. To examine the effect of low-pass filtering on the DNS, the wall pressure of the simulation was sampled at a single spanwise grid point for three streamwise locations: $x/\delta = -6.90$ in the upstream boundary layer, $x/\delta = -2.98$ at the mean separation point, and $x/\delta = -2.18$ near the peak in $p'_{w,\mathrm{rms}}$. The DNS data were generated at a frequency of about 16 MHz and were low-pass filtered in MATLAB using a fourth-order Butterworth filter with a cutoff frequency of 50 kHz to match the experiments. Time traces of the low-pass filtered data at each location are given in Fig. 12c. Figure 11 shows $p'_{w,\mathrm{rms}}$ calculated from these data with and without filtering. The unfiltered point data at $x/\delta = -6.90$ and 2.98 match the DNS data averaged over the full spanwise domain. However, the unfiltered, single-point $p'_{w,\mathrm{rms}}$ at $x/\delta = -2.18$ is higher than the spanwise-averaged data by about 9%. The primary contribution to $p'_{w,\mathrm{rms}}$ at this location comes from the oscillating shock wave, and, because the DNS data contain about three oscillation periods, it is not surprising that the single-point data do not agree with the spanwise-averaged data.

For the upstream data and that at $x/\delta = -2.98$, the low-pass filtering effectively halves the absolute difference between the DNS $p'_{w,\mathrm{rms}}$ curve and that of the experiments. At these streamwise locations, the δ-scale eddies in the upstream turbulent boundary layer, which have a frequency of about 90 kHz, should contribute significantly to $p'_{w,\mathrm{rms}}$. Therefore, it is expected that low-pass filtering the DNS data at these points should decrease the magnitude of $p'_{w,\mathrm{rms}}$ and bring it closer to the experimental value. At $x/\delta = -2.18$, however, the low-pass filtering of the DNS data does not bring the DNS curve significantly closer to the experimental value. The major part of the difference is probably due to the uncorrelated noise described previously, which is amplified through the shock wave. These results indicate that the simple perturbation analysis to estimate the contribution of the uncorrelated noise in the DNS to $p'_{w,\mathrm{rms}}$ probably overpredicts the differences between the experimental and DNS curves. A combination of the limited frequency resolution of the experiments and the larger fluctuation levels of the simulation is the most likely explanation for the differences.

Figure 12 shows wall-pressure signals from the Kulite transducer at different streamwise locations for the present study, along with similar data from the high-Reynolds-number measurements of Dolling and Murphy [3] and the DNS of Wu and Martín [9]. A comparison demonstrates the significant difference between the p_w signals of the high- and low-Reynolds-number data. At the location of the peak in $p'_{w,\mathrm{rms}}$, the wall-pressure signal for the high-Reynolds-number experiment shows the well-documented intermittent behavior: the pressure jumps from the undisturbed boundary-layer value to that behind the shock, and back again, as the shock oscillates over the measurement location. Near the mean separation point, the high-Reynolds-number signal displays peaks of the same magnitude but with a larger average period. In contrast, the wall-pressure data for both the low-Reynolds-number experiment and the DNS do not show this well-defined intermittency. The low-Reynolds-number traces display a broader range of frequencies having amplitudes that are a significant fraction of that due to the low-frequency shock oscillation. This difference is most likely due to the different flow topology of the low-Reynolds-number cases. Both the DNS data and the present FRS visualizations indicate that the shock does not penetrate as far into the boundary layer as it does for high-Reynolds-number flows. For the low-Reynolds-number studies, the shock penetrates about halfway into the boundary layer. Moreover, the DNS shows that a compression fan exists in the shock foot, or separation region, most likely due to the shock being diffused by increased viscous effects. This wave structure merges into the separation shock at approximately half the boundary-layer height [9]. This enriches the wall-pressure signal and attenuates its intermittency, as it is not associated with the motion of a single, well-defined shock wave. The compression fan structure also explains the larger extent of the separation bubble, as well as the smaller value of the peak in $p'_{w,\mathrm{rms}}$. It causes the wall-pressure fluctuations from the shock to be spread over a larger streamwise extent than the high-Reynolds-number case, so that the peak in the streamwise distribution of $p'_{w,\mathrm{rms}}$ is comparatively lower and wider.

A consequence of the attenuated intermittency of the pressure signal is that the algorithms used in high-Reynolds-number studies to

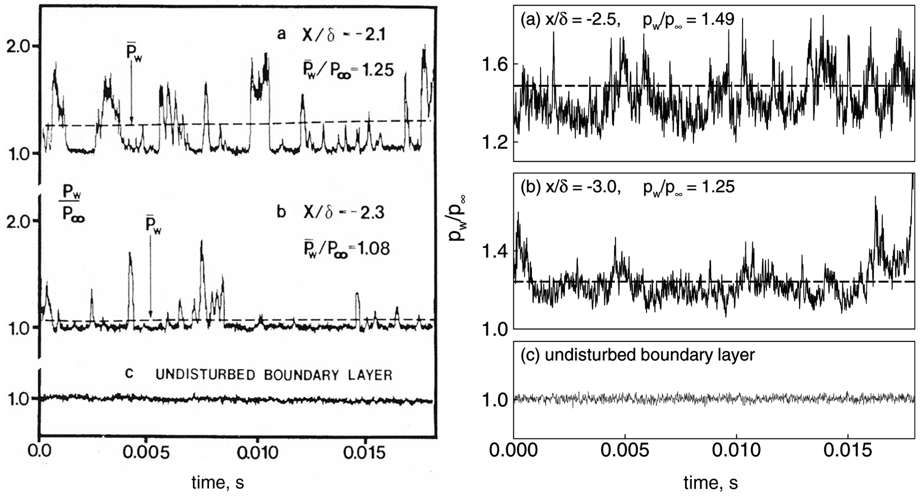

a) From Dolling and Murphy [3] b) Present

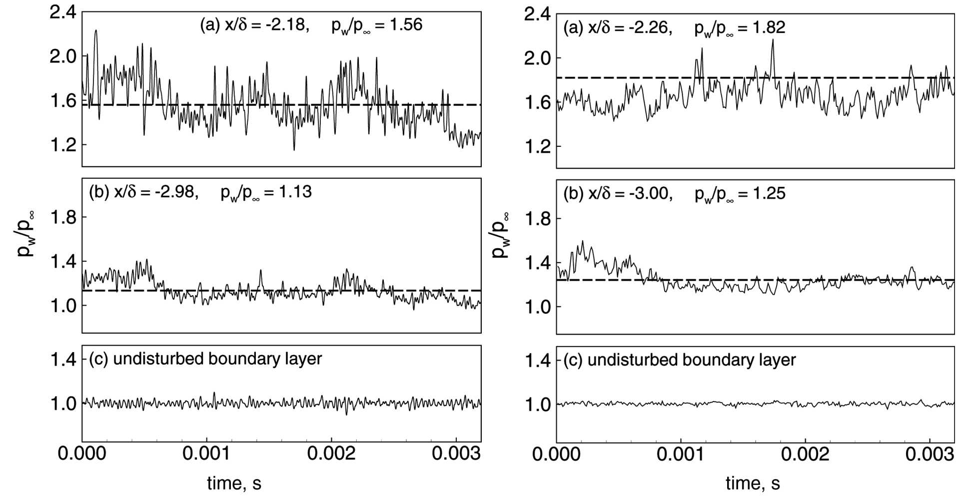

c) Adapted from the DNS of Wu and Martín [9] d) Present

Fig. 12 Comparison of wall-pressure signals at low and high Re_θ for Mach 3: a) adapted from Dolling and Murphy [3], $Re_\theta = 69,100$; b) present data, $Re_\theta = 2400$. Plot ordinate has been stretched so that signal strengths are comparable to those of Fig. 12a; c) created using the DNS of Wu and Martín [9], $Re_\theta = 2300$. Simulation data are low-pass filtered using a fourth-order Butterworth filter, cutoff frequency is 50 kHz ($f\delta/U_\infty = 0.55$) to match the present study; d) present data, same axis ranges as Fig. 12c. Subfigures show data at three locations, from top to bottom: peak in $p'_{w,\mathrm{rms}}$, near the mean separation point, upstream boundary layer. Dashed lines indicate mean values. Figures 12c and 12d are taken from Ringuette and Smits [43].

obtain the shock-motion frequency based on a determination of the shock location (see, for example, Dolling and Brusniak [44]) cannot be directly applied to the present case. In the absence of such methods, frequency information can be obtained from the energy spectrum of the wall-pressure signal. Figure 13a gives an isometric view of the premultiplied power spectral density of the wall-pressure signal at different streamwise locations. The spectra have been smoothed over equal logarithmic bins in frequency, using the dimensional frequency with the entire frequency range divided into 100 bins. The corresponding plot for the high-Reynolds-number experiment of Selig et al. [7] at Mach 2.85 is shown in Fig. 13b. For the high-Reynolds-number case, U_∞/δ is 22 kHz, whereas it is 90 kHz for the present experiment. Both spectra show broadband, low-frequency peaks located in the shock-motion region, which are not present downstream of the shock. Additionally, both cases exhibit peaks in the high-frequency range that appear in the shock region and grow in strength downstream of the shock. The small peaks at $f\delta/U_\infty > 2.7$ in the spectra of Selig et al. [7], downstream of $x/\delta = -1.54$, are not flow related and are due to the resonance of the Kulite transducer.

For the current experiment, the low-frequency peaks corresponding to the shock motion at different streamwise locations have frequencies ranging from about $f\delta/U_\infty = 6.0 \times 10^{-3}$ to 9.0×10^{-3} (0.55–0.82 kHz), whereas they vary from approximately $f\delta/U_\infty = 2.0 \times 10^{-2}$ to 4.5×10^{-2} (0.45–1.0 kHz) for the case of Selig et al. [7]. The dimensional values for the low-Reynolds-number experiment therefore fall within the range of the characteristic shock oscillation frequencies found in the high-Reynolds-number study. Note that the better agreement using the dimensional shock-motion frequency rather than the U_∞/δ scaling stems from the fact that the large-scale shock translation is not caused by the individual large eddies in the incoming boundary layer [12]. We also find good agreement between the low-frequency peak locations for the current experiment and the corresponding DNS of Wu and Martín [24].

The high-frequency peaks for the present experiment occur between $f\delta/U_\infty = 2.1 \times 10^{-1}$ and 3.6×10^{-1} (19 and 33 kHz), and those of Selig et al. [7] are located between about $f\delta/U_\infty = 7.2 \times 10^{-1}$ and 1.3×10^{0} (16 and 30 kHz). Selig et al. [7] comment that, for their high-Reynolds-number flow, pressure fluctuations at frequencies greater than 10 kHz ($f\delta/U_\infty = 4.5 \times 10^{-1}$) are due purely to turbulent fluctuations, but below this value there is an overlap between frequencies corresponding to both turbulence and the shock motion. Using this nondimensional frequency as an approximate cutoff, the overlap region of the present experiment extends nearly to the highest resolved frequency. Figure 13 shows that the high-frequency pressure fluctuations become more energetic

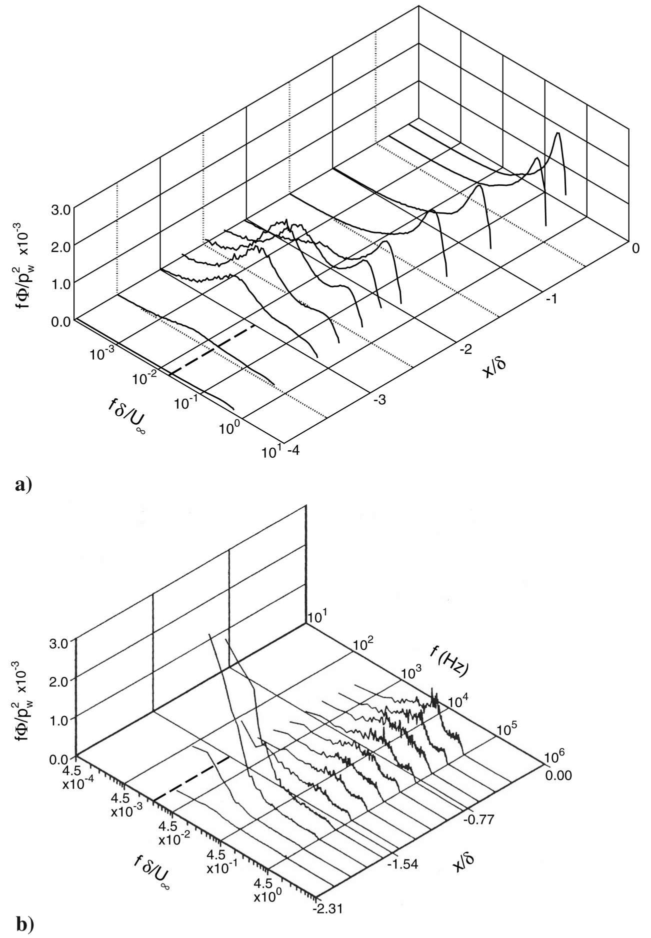

Fig. 13 Energy spectra of the wall-pressure signal at multiple streamwise locations upstream of the corner ($x/\delta = 0$). Frequency is nondimensionalized using U_∞/δ: a) present data, Mach 2.9, $Re_\theta = 2400$, $\delta/U_\infty = 1.1 \times 10^{-5}$; b) adapted from Selig et al. [7], Mach 2.85, $Re_\theta = 84{,}500$, $\delta/U_\infty = 4.5 \times 10^{-5}$. A dashed line has been added to both plots to indicate the lowest nondimensional frequency resolved by the measurements of Selig et al. [7].

downstream of the shock for both the high- and low-Reynolds-number studies, so that the present data are consistent with the well-established high-Reynolds-number result that the turbulent motions are amplified across the interaction [6]. For the high-Reynolds-number flow of Selig et al. [7], U_∞/δ (22 kHz) falls within the range of the Kulite transducer used, whereas for the present experiment (90 kHz) it does not. Therefore, the wall-pressure spectra for the current work drop off before U_∞/δ is reached, and the large-eddy frequency scaling does not appear to collapse the high-frequency data for the two studies. Presumably, the collapse would be better if the large-eddy frequency for the low-Reynolds-number measurements were resolved. Although frequencies near U_∞/δ are not captured for the present case, frequencies two decades below that measured by Selig et al. [7] are. This observation illustrates the limited bandwidth of the transducers used, and how it shifts in nondimensional frequency depending on the flow conditions (see the dashed line in Fig. 13).

Figure 13 shows that the most significant difference between the low- and high-Reynolds-number data, which were normalized in the same way, is that the low-Reynolds-number peaks corresponding to the shock motion are smaller in magnitude. For the high-Reynolds-number case, the energy of the peaks due to the shock motion is about 3 times that of the turbulence. The shock-motion peaks at low-Reynolds-number are comparable in magnitude to the higher-frequency peaks, although the low-pass filtering of frequencies greater than 50 kHz ($f\delta/U_\infty = 5.5 \times 10^{-1}$) (see Sec. II.B) reduces the energy of the higher-frequency fluctuations, so that their true energy is greater than shown. These results are consistent with the wall-pressure signals shown in Fig. 12. The higher degree of intermittency due to the deeper penetration of the shock wave in the high-Reynolds-number boundary layer causes more energy to be concentrated at the frequencies associated with the shock motion. In contrast, the more continuous amplitudes of the pressure signal for the low-Reynolds-number flow, presumably a result of the diffusion of the separation shock into a compression fan structure in the lower-half of the boundary layer, cause the energy in the wall-pressure spectra to be distributed over a greater range of frequencies. This reduces the magnitudes of the spectral peaks associated with the shock motion.

IV. Conclusions

A Mach 2.9 shock wave turbulent boundary-layer interaction with a low Reynolds number based on momentum thickness of 2400 was studied experimentally. Mean flow surveys, flow visualization, and fluctuating wall-pressure measurements were conducted. Compared with previous data at higher Reynolds numbers (of order 10^4–10^5), the separation bubble in the corner region is a factor of 2 larger than the high-Reynolds-number results, and the peak in the rms of the wall-pressure fluctuations is about a factor of 2 smaller. The wall-pressure signal does not contain the distinct intermittency that is characteristic of high-Reynolds-number data in the shock-foot region. Moreover, the wall-pressure spectra show that the energy of the fluctuations is more evenly distributed over the range of shock-motion frequencies. This results in a smaller peak energy in the shock oscillation region than is observed at high Reynolds numbers.

These differences are most likely due to the change in flow characteristics at the low-Reynolds-number, namely, the spread of the separation shock into a compression fan in the lower-half of the boundary layer, and a taller separation bubble. One contributing factor is the relative change in the sonic line location. For the present experiments, a curve fit to the Mach number profile in the upstream boundary layer indicated that the sonic line was located at about 0.06δ away from the wall ($y^+ \approx 20$). The DNS of Wu and Martín [9] gives a very similar value of 0.05δ. For the high-Reynolds-number investigation of Settles [36], the sonic line is about a factor of 10 lower than the low-Reynolds-number values in terms of outer scaling (0.006δ), although the distance in wall units is closer ($y^+ \approx 53$). At the low Reynolds number, the viscous region near the wall occupies a significant fraction of the boundary layer; if it is assumed that the viscous part of the layer ends at $y^+ = 50$, this represents about 15% of the boundary-layer thickness. It appears that one result is the increase in separation bubble size observed, as the relatively stronger effect of viscous forces exacerbates the flow separation (note that, in all laminar flows, the separation region is very much larger than in turbulent flows). The DNS of Wu and Martín [24] shows that the separation bubble extends to about 0.5δ away from the wall, whereas in the high-Reynolds-number experiments of Settles et al. [45], the height of the separation bubble is about 0.2δ, where δ is the incoming boundary-layer thickness. In addition, the DNS shows that the separation shock is spread into a compression fan below a wall-normal distance of about 0.5δ. As discussed earlier, the compression fan structure is the most likely reason for the enrichment of the low-Reynolds-number wall-pressure signal [Figs. 12c and 12d] and its attenuated intermittency. Moreover, it explains the relatively lower and broader peaks due to the shock motion in the energy spectra of the wall pressure.

In terms of turbulence structure, the average turbulent structure angle decreases slightly (compared to the undisturbed boundary-layer value) at 0.5δ upstream of the interaction, consistent with the high-Reynolds-number results of Donovan et al. [42] in the initial compression region of a supersonic boundary layer perturbed by concave curvature.

The shock motion has a broadband frequency distribution with a peak at slightly less than 1 kHz, as seen in the high-Reynolds-number data. As expected, scaling the shock-motion frequency using that of the large eddies in the incoming boundary layer U_∞/δ does not collapse the low- and high-Reynolds-number data, suggesting that an alternative scaling is more appropriate.

We find good agreement with the DNS of Wu and Martín [9] at matching conditions, namely in the mean flow surveys, the rms of the wall-pressure fluctuations, the behavior of the wall-pressure signal, and the shock-motion frequency. The rms pressure-fluctuation profile of the DNS is somewhat higher due to uncorrelated pressure fluctuations, or noise, introduced at the initialization of the simulation.

Acknowledgments

We would like to acknowledge the support from the U.S. Air Force Office of Scientific Research under grant no. FA 9550-06-1-0323. We would also like to thank Noel Clemens, Pablo Bueno, and Frank Wise of the University of Texas at Austin, Glenn Atkinson of the Princeton University Physics Department machine shop, and Christina Peabody for their help with the design of the Kulite transducer holder and supporting electronics. We are grateful for the help of William Stokes on the experimental setup and running the tunnel, Zhilei Wu for assistance in operating the facility, and Pino Martín for allowing us access to her direct numerical simulation database.

References

[1] Settles, G. S., Bogdonoff, S. M., and Vas, I., "Incipient Separation of a Supersonic Turbulent Boundary Layer at High Reynolds Numbers," *AIAA Journal*, Vol. 14, No. 1, 1976, pp. 50–56. doi:10.2514/3.61331

[2] Settles, G. S., Fitzpatrick, T. J., and Bogdonoff, S. M., "Detailed Study of Attached and Separated Compression Corner Flowfields in High Reynolds Number Supersonic Flow," *AIAA Journal*, Vol. 17, No. 6, 1979, pp. 579–585. doi:10.2514/3.61180

[3] Dolling, D. S., and Murphy, M. T., "Unsteadiness of the Separation Shock Wave Structure in a Supersonic Compressible Ramp Flowfield," *AIAA Journal*, Vol. 21, No. 12, 1983, pp. 1628–1634. doi:10.2514/3.60163

[4] Ardonceau, P. L., "The Structure of Turbulence in a Supersonic Shock Wave/Boundary Layer Interaction," *AIAA Journal*, Vol. 22, No. 9, 1984, pp. 1254–1262. doi:10.2514/3.48565

[5] Kuntz, D. W., Amatucci, V. A., and Addy, A. L., "Turbulent Boundary-Layer Properties Downstream of the Shock Wave/Boundary-Layer Interaction," *AIAA Journal*, Vol. 25, No. 5, 1987, pp. 668–675. doi:10.2514/3.9681

[6] Smits, A. J., and Muck, K.-C., "Experimental Study of Three Shock Wave/Turbulent Boundary Layer Interactions," *Journal of Fluid Mechanics*, Vol. 182, 1987, pp. 291–314. doi:10.1017/S0022112087002349

[7] Selig, M. S., Muck, K.-C., Dussauge, J. P., and Smits, A. J., "Turbulence Structure in a Shock Wave/Turbulent Boundary-Layer Interaction," *AIAA Journal*, Vol. 27, No. 7, 1989, pp. 862–869. doi:10.2514/3.10193

[8] Adams, N. A., "Direct Simulation of the Turbulent Boundary Layer Along a Compression Ramp at $M = 3$ and $Re_\theta = 1685$," *Journal of Fluid Mechanics*, Vol. 420, 2000, pp. 47–83. doi:10.1017/S0022112000001257

[9] Wu, M., and Martín, M. P., "Direct Numerical Simulation of Supersonic Turbulent Boundary Layer over a Compression Ramp," *AIAA Journal*, Vol. 45, No. 4, 2007, pp. 879–889. doi:10.2514/1.27021

[10] Andreopoulos, J., and Muck, K.-C., "Some New Aspects of the Shock Wave Boundary-Layer Interaction in Compression Ramp Flows," *Journal of Fluid Mechanics*, Vol. 180, 1987, pp. 405–428. doi:10.1017/S0022112087001873

[11] Muck, K.-C., Andreopoulos, J., and Dussauge, J. P., "Unsteady Nature of Shock Wave/Turbulent Boundary-Layer Interaction," *AIAA Journal*, Vol. 26, No. 2, 1988, pp. 179–187. doi:10.2514/3.9870

[12] Erengil, M. E., and Dolling, D. S., "Correlation of Separation Shock Motion with Pressure Fluctuations in the Incoming Boundary Layer," *AIAA Journal*, Vol. 29, No. 11, 1991, pp. 1868–1877. doi:10.2514/3.10812

[13] Beresh, S. J., Clemens, N. T., and Dolling, D. S., "Relationship Between Upstream Turbulent Boundary Layer Velocity Fluctuations and Separation Shock Unsteadiness," *AIAA Journal*, Vol. 40, No. 12, 2002, pp. 2412–2422. doi:10.2514/2.1609

[14] Hutchins, N., and Marusic, I., "Evidence of Very Long Meandering Features in the Logarithmic Region of Turbulent Boundary Layers," *Journal of Fluid Mechanics*, Vol. 579, 2007, pp. 1–28. doi:10.1017/S0022112006003946

[15] Kim, K. C., and Adrian, R. J., "Very Large-Scale Motion in the Outer Layer," *Physics of Fluids*, Vol. 11, No. 2, 1999, pp. 417–422. doi:10.1063/1.869889

[16] Ganapathisubramani, B., Clemens, N. T., and Dolling, D. S., "Effects of Upstream Boundary Layer on the Unsteadiness of Shock-Induced Separation," *Journal of Fluid Mechanics*, Vol. 585, 2007, pp. 369–394. doi:10.1017/S0022112007006799

[17] Ringuette, M. J., Wu, M., and Martín, M. P., "Coherent Structures in Direct Numerical Simulation of Turbulent Boundary Layers at Mach 3," *Journal of Fluid Mechanics*, Vol. 594, 2008, pp. 59–69. doi:10.1017/S0022112007009020

[18] Ganapathisubramani, B., Clemens, N., and Dolling, D., "Large-Scale Motions in a Supersonic Turbulent Boundary Layer," *Journal of Fluid Mechanics*, Vol. 556, 2006, pp. 271–282. doi:10.1017/S0022112006009244

[19] Jiménez, J., "The Largest Scales of Turbulent Wall Flows," *Center for Turbulence Research, Annual Research Briefs*, Stanford Univ., Stanford, CA, 1998, pp. 137–154.

[20] Balakumar, B. J., and Adrian, R. J., "Large- and Very-Large-Scale Motions in Channel and Boundary Layer Flows," *Philosophical Transactions of the Royal Society of London, Series A: Mathematical and Physical Sciences*, Vol. 365, No. 1852, 2007, pp. 665–681. doi:10.1098/rsta.2006.1940

[21] Thomas, F. O., Putnam, C. M., and Chu, H. C., "On the Mechanism of Unsteady Shock Oscillation in Shock Wave/Turbulent Boundary Layer Interactions," *Experiments in Fluids*, Vol. 18, Nos. 1–2, 1994, pp. 69–81. doi:10.1007/BF00209362

[22] Smits, A. J., and Dussauge, J.-P., *Turbulent Shear Layers in Supersonic Flow*, 2nd ed., Springer, New York, 2006.

[23] Dussauge, J.-P., Dupont, P., and Debíeve, J.-F., "Unsteadiness in Shock Wave Boundary Layer Interactions with Separation," *Aerospace Science and Technology*, Vol. 10, No. 2, 2006, pp. 85–91. doi:10.1016/j.ast.2005.09.006

[24] Wu, M., and Martín, M. P., "Analysis of Shock Motion in Shockwave and Turbulent Boundary Layer Interaction Using Direct Numerical Simulation Data," *Journal of Fluid Mechanics*, Vol. 594, 2008, pp. 71–83.

[25] Ringuette, M. J., Wu, M., and Martín, M. P., Low Reynolds Number Effects in a Mach 3 Shock/Turbulent-Boundary-Layer Interaction," *AIAA Journal*, Vol. 46, No. 7, 2008, pp. 1884–1887. doi:10.2514/1.36213

[26] Bookey, P., "An Experimental Study of Shock/Turbulent Boundary Layer Interactions at DNS Accessible Reynolds Numbers," Master's Thesis, Princeton Univ., Princeton, NJ, 2005.

[27] Raman, K. R., "A Study of Surface Pressure Fluctuations in Hypersonic Turbulent Boundary Layers," NASA CR 2386, Feb. 1974.

[28] Dolling, D. S., and Dussauge, J. P., "Fluctuating Wall-Pressure Measurements," Chap. 8, AGARD AG-315, 1989.

[29] Corcos, G. M., "Resolution of Pressure in Turbulence," *Journal of the Acoustical Society of America*, Vol. 35, No. 2, 1963, pp. 192–199. doi:10.1121/1.1918431

[30] Erbland, P. J., "Filtered Rayleigh Scattering and Homogeneous Nucleation of CO_2 in Supersonic Flows," Ph.D. Thesis, Princeton Univ., Princeton, NJ, 2000.

[31] Forkey, J. N., "Development and Demonstration of Filtered Rayleigh Scattering: A Laser Based Flow Diagnostic for Planar Measurement of Velocity, Temperature and Pressure," Ph.D. Thesis, Princeton Univ., Princeton, NJ, 1996.

[32] van Driest, E. R., "On Turbulent Flow near a Wall," *Journal of the Aeronautical Sciences*, Vol. 23, No. 11, 1956, pp. 1007–1011, 1036.

[33] Clauser, F. H., "The Turbulent Boundary Layer," *Advances in Applied Mechanics*, Vol. 4, Academic Press, New York, 1956, pp. 1–51.

[34] Spalding, D. B., and Chi, S. W., "The Drag of a Compressible Turbulent Boundary Layer on a Smooth Flat Plate with and Without Heat Transfer," *Journal of Fluid Mechanics*, Vol. 18, 1964, pp. 117–143. doi:10.1017/S0022112064000088

[35] Allen, J. M., "Pitot-Probe Displacement in a Supersonic Turbulent Boundary Layer," NASA TN D-6759, 1972.

[36] Settles, G. S., "An Experimental Study of Compressible Turbulent Boundary Layer Separation at High Reynolds Number," Ph.D. Thesis, Princeton Univ., Princeton, NJ, 1975.

[37] Zheltovodov, A., Schulein, E., and Horstman, C., "Development of Separation in the Region Where a Shock Interacts with a Turbulent

Boundary Layer Perturbed by Rarefaction Waves," *Journal of Applied Mechanics and Technical Physics*, Vol. 34, No. 3, 1993, pp. 346–354. doi:10.1007/BF00864786

[38] Selig, M. S., "Unsteadiness of Shock Wave/Turbulent Boundary Layer Interactions with Dynamic Control," M.S.E. Thesis, Princeton Univ., Princeton, NJ, 1988.

[39] Klebanoff, P., "Characteristics of Turbulence in a Boundary Layer with Zero Pressure Gradient," NACA TR 1247, 1955.

[40] Spina, E. F., Donovan, J. F., and Smits, A. J., "On the Structure of High-Reynolds Number Supersonic Turbulent Boundary Layers," *Journal of Fluid Mechanics*, Vol. 222, 1991, pp. 293–327. doi:10.1017/S0022112091001118

[41] Fitzgibbon, A. W., Pilu, M., and Fisher, R. B., "Direct Least Squares Fitting of Ellipses," *IEEE Transactions on Pattern Analysis and Machine Intelligence*, Vol. 21, No. 5, May 1999, pp. 476–480. doi:10.1109/34.765658

[42] Donovan, J. F., Spina, E. F., and Smits, A. J., "The Structure of a Supersonic Turbulent Boundary Layer Subjected to Concave Surface Curvature," *Journal of Fluid Mechanics*, Vol. 259, 1994, pp. 1–24. doi:10.1017/S0022112094000017

[43] Ringuette, M. J., and Smits, A. J., Wall Pressure Measurements in a Mach 3 Shock-Wave Turbulent Boundary Interaction at a DNS-Accessible Reynolds Number, AIAA Paper 2007-4113, 2007.

[44] Dolling, D. S., and Brusniak, L., "Separation Shock Motion in Fin, Cylinder, and Compression Ramp-Induced Turbulent Interactions," *AIAA Journal*, Vol. 27, No. 6, 1989, pp. 734–742. doi:10.2514/3.10173

[45] Settles, G. S., Vas, I., and Bogdonoff, S. M., "Details of a Shock Separated Turbulent Boundary Layer at a Compression Corner," *AIAA Journal*, Vol. 14, No. 12, 1976, pp. 1709–1715. doi:10.2514/3.61513

N. Chokani
Associate Editor